The effect of phosphorous content on the microstructure and localised corrosion of electroless nickel-coated copper

Mousavi, M.; Rahimi, E.; Mol, J. M.C.; Gonzalez-Garcia, Y.

DOI
10.1016/j.surfcoat.2024.131174

Publication date
2024

Document Version
Final published version

Published in
Surface and Coatings Technology

Surface & Coatings Technology 492 (2024) 131174

Contents lists available at ScienceDirect

Surface & Coatings Technology

journal homepage: www.elsevier.com/locate/surfcoat

The effect of phosphorous content on the microstructure and localised corrosion of electroless nickel-coated copper

M. Mousavi *, E. Rahimi, J.M.C. Mol, Y. Gonzalez-Garcia

Department of Materials Science and Engineering, Delft University of Technology, Mekelweg 2, 2628 CD Delft, the Netherlands

ARTICLE INFO

Keywords:
Metallic coating
Electroless NiP
Corrosion
Microstructure
Potentiodynamic polarisation
SKPFM

ABSTRACT

A detailed microstructural and electrochemical analysis of electroless nickel phosphorous (NiP) coatings with P contents of 13.2 ± 1.2 wt%, 12.9 ± 0.7 wt%, and 8.3 ± 0.8 wt% on a copper substrate was performed to study the corrosion behaviour of electroless NiP/Cu systems. The P content of the electroless NiP coatings plays an essential role in the microstructure of the coatings in terms of crystallinity. The crystallinity variations, representing the extent of crystalline and amorphous phases within the material, with P content, affect the local electrochemical characteristics and, hence, the corrosion protection behaviour of electroless NiP coatings. The coatings with the highest P content showed the best corrosion performance in a 3.5 wt-% NaCl solution. In contrast, the surface of the electroless NiP coatings with low P content is more susceptible to corrosion due to the presence of locations with heterogeneous electronic properties that initiate localised corrosion. Microgalvanic interactions with a high cathode-to-anode surface ratio govern the localised corrosion kinetics of the low P-content samples. A high concentration of nodule boundaries and/or other existing structural defects on the surface serve as anodic sites, whereas the remainder of the surface serves as cathodic sites.

1. Introduction

Metallic coatings are of significant practical and technological importance in our daily lives as functional or protective surface coverage concepts [1]. As a widely used metallic coating, electroless nickel (EN) is a chemical or auto-catalytic plating process that involves depositing a layer of nickel onto the surface substrate, typically a metal or plastic component [2]. EN coatings offer several advantages, including uniform and controlled deposition [3], good wear and corrosion performance, high hardness, improved electrical conductivity, and good solderability [4,5]. The versatility and ease of application of EN coatings have made them extensively used in several industrial sectors, including renewable energy applications [6–8], automotive [9], aerospace [10,11], biomedical [12], oil and gas [13,14], and electronics industries [15–20].

The use of EN coatings on copper substrates for electronic applications has become increasingly prevalent due to addressing the specific and strict requirements of the electronic industry such as safety measures and high-performance reliability. This is particularly crucial given copper's high susceptibility to oxidation. EN coatings are utilised in the electronic industry as an intermediate coating between the copper substrate and gold top layer in the electroless nickel immersion gold (ENIG) coating system for printed circuit boards (PCBs). PCBs with EN coatings are ideal for high-wear applications like connectors and switches and can withstand exposure to harsh environments. Additionally, EN coatings offer good solderability, which is important for assembling PCBs [21,22]. The intermediate EN coating in PCBs prevents copper and gold interdiffusion [17]. However, the performance of EN coatings can be significantly affected by various factors, such as the composition, electronic properties, microstructure, and deposition conditions of the coating.

The presence of P, as the predominant alloying element in electroless NiP coatings, notably influences the microstructure of the coatings in terms of crystallinity level. Depending on the P content, the microstructure of electroless NiP coatings has been found to be either amorphous, crystalline, or both. Crystalline (β), mixed amorphous crystalline (β and γ coexist), and amorphous (γ) phases have been reported for coatings with low (3–5 wt-%), medium (6–10 wt-%), and high (11–18 wt-%) P contents, respectively [23,24]. Electroless NiP coatings are less porous, have a more uniform thickness, and are harder than the corresponding P-less electroplated nickel coating [24–26]. Moreover, the P content in the EN coating substantially impacts the corrosion protection performance of the coating. In addition to their passive nature, the

* Corresponding author.
E-mail address: m.mousavi-1@tudelft.nl (M. Mousavi).

https://doi.org/10.1016/j.surfcoat.2024.131174
Received 24 February 2024; Received in revised form 25 June 2024; Accepted 23 July 2024
Available online 5 August 2024

mentioned unique properties of electroless NiP coatings make them excellent at resisting corrosion in various environments, such as neutral and acidic conditions, where a higher P content (above 10 wt-%) is advantageous, as well as in strong alkaline media, where coatings with lower phosphorus content are more effective [4]. Electroless Ni coatings with a high P concentration provide superior corrosion protection, whereas those with a moderate or low P content perform poorly in neutral or acidic corrosive environments. Due to the absence of grains and grain boundaries, which are often sites of corrosion attack in crystalline materials, amorphous alloys exhibit superior corrosion resistance compared to equivalent polycrystalline materials [27,28]. This is not the only mechanism known for the enhanced corrosion protection provided by high-phosphorus content coatings in the literature. As mentioned in Pedrizzetti et al.'s work [25], preferential Ni dissolution enriches the surface with phosphorus, promoting the formation of stable Ni3P and NixPy compounds. These compounds create a pseudo-passive barrier layer on the surface, thereby hindering further corrosion.

Microstructural and electrochemical studies on various substrates, including mild steel, twinning-induced plasticity (TWIP) steel, AZ31 Mg alloy, and aluminium alloy 2024-T3, have been conducted to investigate the impact of P content on the corrosion protection of electroless NiP coatings [10,24,30–32]. Shibli and Dilimon [30] investigated the microstructural and morphological effects of P content and TiO_2-reinforcement on electroless NiP coatings for hydrogen evolution reactions on mild steel. In terms of microstructure, they concluded that the electroless NP-coated surface with low P content shows Ni (111) and Ni (200) lattice structures with distinct peaks, revealing the crystalline nature as shown by X-ray diffraction (XRD). On the other hand, in the case of medium P content, they detected more blurry and diffused diffraction peaks. Most notably, no diffraction peaks were observed for the electroless NiP plates with high P content due to their amorphous structure. The disordered lattice caused by an increase in the P content of the plates may have resulted in a transition from a crystalline to an amorphous texture. Regarding the morphological integrity of electroless NiP surfaces, coatings with high P content showed a defect-free top-surface morphology, while those with medium content showed distinguished nodules. Medium P content coatings also displayed porous surfaces. Coatings with low P content exhibited porous surfaces, non-uniform nodular sizes, irregular nodular boundaries, and minor defects.

Numerous studies have demonstrated that the addition of phosphorus to electroless nickel coatings enhances their corrosion performance in neutral or acidic conditions by increasing the tendency for passivation and forming stable intermediate compounds (Ni_xP_y) [4,23,24,28,30,33–36]. Bai et al. [33] investigated the corrosion behaviour of electroless Ni-P coatings with supersaturated P contents of 20, 24, and 28 at.% in chlorine-containing corrosive media by accelerated electrochemical techniques and a brine-fog method. They concluded that the P content has a substantial impact on the corrosion rate in brine media. They demonstrated that an increased P content results in a positive shift in the corrosion potential and a reduction in the corrosion current density. In addition, they demonstrated that the corrosion rate of the coatings depends significantly on the annealing temperature. Bonin et al. [35] studied the corrosion behaviour of electroless nickel-boron-phosphorous duplex coatings on mild steel in different corrosion media. They demonstrated that a hypophosphite layer is generated during anodic polarisation in a 3.5 wt-% NaCl solution at a pH of 5.9. Ni hydration is impeded by the formation of a hypophosphite layer, which prevents the electrolyte from reaching and interacting with the Ni electrode surface.

Furthermore, there are many studies in the recent literature about enhancing the corrosion resistance of electroless NiP-coated substrates by introducing novel composite coatings such as Ni-P-ZnO [37], NiP-C_3N_4/ZnO [38], NiP-TiO_2-ZrO_2 [39], Ni-P-NiTi [40], NiMoP [41], Ni-WP [42], etc. For instance, Chintada and Koona [37] investigated the impact of heat treatment temperature, the quantity of ZnO nanoparticles on microhardness, and the corrosion behaviour of electroless NiP coatings on mild steel. They found that when ZnO nanoparticles were added to the electroless bath up to an amount of 2 g/L, the pores in the Ni-P lattice were filled, and the electrochemically active area of the composite coatings was reduced, leading to improved corrosion performance.

To the best of the authors' knowledge, no prior research has thoroughly explored the impact of P content on the corrosion behaviour of electroless NiP coatings. This study introduces a novel approach by integrating surface analysis, local surface potential measurements, and combined AC/DC electrochemical methods to investigate this aspect comprehensively. Rather than solely aiming at optimising coating performance and deposition parameters, the focus is on unravelling the local corrosion mechanisms at varying P contents and microstructural variations. Through this combined methodology, insights into localised corrosion processes are revealed, shedding light on the driving forces behind corrosion initiation on metallic surfaces. This integration not only elucidates the spatial distribution of anodic and cathodic reactions but also identifies potential locations for corrosion initiation, providing invaluable insights into the effects of local microstructural variations on local corrosion susceptibility [43]. The obtained data can aid in comprehending micrometer-to-nanometer scale localised corrosion and galvanic activities. In scanning Kelvin probe force microscopy (SKPFM) studies for corrosion behaviour applications, differences in work function among microstructural features of the studied surface result in distinct lateral variations in Volta potential. These variations potentially offer valuable insights into the electrochemical characteristics of the materials, particularly in distinguishing anodic and cathodic behaviours. Benaioun et al. [44] employed the SKPFM technique to directly measure the difference in work function values between the sample surface and the tip. This allowed for detailed chemical analysis at a microscopic level. Their use of SKPFM yielded critical insights into the development of passive films, revealing a uniform surface potential across the analysed surfaces.

This study provides a fundamental insight into the local corrosion behaviour of electroless NiP coatings with P contents of 13.2 ± 1.2 wt%, 12.9 ± 0.7 wt%, and 8.3 ± 0.8 wt% on copper substrates in an aqueous chloride-containing environment. Using scanning electron microscopy/energy-dispersive X-ray (SEM/EDS) spectroscopy, focused ion beam (FIB), X-ray diffraction (XRD), atomic force microscopy (AFM), and SKPFM measurements, the as-received samples were characterised in terms of their microstructural, compositional and topographical properties, and their local Volta potential difference distribution. For corrosion performance testing under immersed conditions, potentiodynamic polarisation (PDP) measurements were performed. Also, open-circuit potential (OCP), linear polarisation resistance (LPR), and electrochemical impedance spectroscopy (EIS) measurements were performed over a prolonged period of immersion to study their temporally resolved behaviour.

2. Experimental procedures

2.1. Materials and sample preparation

A commercially operated bath based on nickel hypophosphite was used to deposit electroless NiP coatings of varying P contents onto commercially pure copper sheet (purity >99.9 wt-%). The dimensions of each copper plate were approximately 0.1 cm × 30 cm × 30 cm. The three electroless NiP samples used in this study were named as NP-a, NP-b, and NP-c, corresponding to their P content of 13.2 ± 1.2 wt%, 12.9 ± 0.7 wt%, and 8.3 ± 0.8 wt%, respectively.

2.2. Microstructural and compositional analysis

2.2.1. SEM/EDS

A scanning electron microscopy (SEM) with an energy-dispersive X-ray spectroscopy (EDS) detector (Jeol JSM-IT100) was used to analyse

the morphology and chemical composition of both the as-received and post-corroded samples. Secondary electron imaging (SEI) (was used to map the top-view morphology. The accelerating voltage was 20 keV. An ultrasonic bath (Emag Emmi 20HC) was used to clean the samples by immersing them in isopropanol (IPA) for 10 min before drying them with compressed air.

2.2.2. PFIB

Using plasma-focused ion beam (PFIB) microscopy, the cross-section of the as-received electroless NiP coatings was examined. Utilising a Thermo Scientific™ Helios™ UXe DualBeam G4 PFIB microscope. The surface imaging voltage was set at 5 keV, whereas the EDS measurement voltage was 20 keV. Each is operating in high-resolution SE mode. To protect the surface, the blind mode for FIB sectioning was chosen and ion-beam milling was performed.

2.2.3. XRD

The crystallinity of the coatings was investigated by X-ray diffraction (XRD) analysis. Bragg-Brentano geometry was employed using Cu/K radiation and an X-ray diffractometer (Bruker D8 Advance) equipped with a graphite monochromator and a Vantec position-sensitive detector. Divergence slit Var12, scatter screen height 5 mm, 45 kV 35 mA. The XRD analysis was performed using a scan range (2) of 20 to 120°, a step size of 0.050°, and a dwell time of 0.5 s. The Full Width at Half Maximum (FWHM) values were used to determine the grain sizes using the Scherrer equation [45]:

$$D = \frac{0.94\,\lambda}{\beta\,cos\theta} \tag{1}$$

D represents the average size of the crystallites, β is the width of the diffraction peak at half its maximum intensity, θ denotes the Bragg angle, and λ is the wavelength of the X-ray used.

2.2.4. SKPFM

The SKPFM technique has a high spatial resolution and enables to map the Volta potential distribution over a heterogeneous surface microstructure. The SKPFM technique measures Volta potential difference (VPD) values between a conductive tip and the sample surface. The volta potential values of a conductive sample surface are due to the diverse work function energies of the studied sample and the measuring tip, as explained by the following equation:

$$\Delta V_{(sample/tip)} = \frac{\left(\varnothing_{tip} - \varnothing_{Sample}\right)}{-e} \tag{2}$$

where ϕ_{tip} and ϕ_{sample} are the Work Functions Energies (WFE) of the tip and sample, and e is the electronic charge.

The VPD distribution of a metallic coating surface is reported to be a potential indicator of places prone to the formation of localised corrosion and micro-galvanic couples due to surface heterogeneity and diverse surface features; however, a direct correlation between VPD distribution and micro-galvanic couple formation is not straightforward [46]. To have an insight into the corrosion behaviour of electroless NiP coatings, the electronic properties of the electroless NiP surface in terms of charge distribution and volta potential mapping at the nanoscale level SKPFM measurements were carried out. The SKPFM device used in this study was a Bruker Dimension Edge with an n-type doped silicon pyramid single crystal tip, coated with PtIr5 (SCM-Pit probe). The VPD maps were captured using the dual-scan mode. In the first scan, surface topography data was obtained using tapping mode. Topography and VPD maps were performed in the air at 21° Cwith an approximate relative humidity of 24 %, a pixel resolution of 512 × 512, a zero-bias voltage, and a scan frequency rate of 0.3 Hz. The amplitude of the AC voltage applied to the tip was 6 V. To mitigate the possibility of inaccurate measurements caused by the sensitivity of the technique, this study used the identical measuring tip throughout the whole set of measurements on the same day. For the top-view AFM/SKPFM measurements of as-received electroless NiP coatings, the same cleaning procedure of SEM/EDS measurements was applied. For cross-sectional AFM/SKPFM measurements of the thickness of the electroless NiP coatings, the as-received samples were embedded in an epoxy resin and ground to 4000 grit with SiC sanding paper. Afterwards, the samples were polished with a fine diamond suspension (Struers DiaDua-2) with particle sizes of 3 μm and 1 μm. The cross-sectional AFM/SKPFM measurements of the electroless NiP coatings were performed in the electroless NiP/Cu interface region. Therefore, the histogram analysis based on the multimodal Gaussian distributions was employed for a more detailed interpretation of the VPD values at the electroless NiP/Cu interface.

2.3. Electrochemical analysis

A Biologic SP 300 multichannel potentiostat was used for all electrochemical measurements hereafter. A typical three-electrode cell consisting of an Ag/AgCl electrode (saturated KCl) as the reference electrode, platinum mesh as the auxiliary electrode, and electroless NiP samples as the working electrode. A circular area of the electroless NiP surface with a diameter of 10 mm was exposed to the corrosive media. PDP, OCP, LPR, and EIS measurements were performed in an aqueous electrolyte solution of 3.5 wt-% NaCl. The electroless NiP coatings were cleaned in an ultrasonic bath (Emag Emmi 20HC) for 10 min during immersion in isopropanol and then dried with compressed air prior to all measurements.

2.3.1. PDP

Potentiodynamic polarisation tests were performed after an OCP stabilisation time of 25 min. PDP measurements were conducted in the potential range of −0.25 V to 0.50 V (vs. OCP) at a scan rate of 1 mV/s. The EC-Lab V11.33 software was utilised to extrapolate the Tafel curves. The reproducibility of the results was evaluated by performing the tests in triplicate.

2.3.2. OCP and LPR

Open circuit potential and linear polarisation resistance measurements were used to determine the temporally resolved corrosion behaviour of the as-received electroless NiP coatings over 72 h of immersion in a 3.5 wt-%NaCl solution. In a potential range of ±10 mV around the open circuit potential, LPR measurements were performed intermittently, i.e., every hour for the initial 12 h and subsequently every 3 h until the experiment reaches the 72-hour immersion mark). The scan rate was 0.167 mV/s. The samples were rinsed with Milli-Q® ultrapure water and dried with compressed clean air following 72 h of immersion in a 3.5 wt-% NaCl solution for morphological and compositional analysis of post-corroded samples. The lower LPR scan rate compared to PDP is due to the focus on accurate, stable measurements of corrosion resistance within a limited potential range, minimizing perturbation of the system. The scan rate for LPR was chosen relatively low to ensure precise measurements of polarisation resistance, while for PDP tests, a faster scan rate was employed to capture dynamic corrosion processes across a wider potential range, facilitating the identification of critical thresholds and kinetic characteristics of the coating.

2.3.3. EIS

Electrochemical impedance spectroscopy (EIS), an additional non-destructive electrochemical characterisation technique, was utilised to assess the corrosion performance of electroless NiP coatings temporally. An AC signal of 10 mV amplitude was applied to the working electrode at the E_{OCP} to determine the electrochemical impedance. The impedance measurements were performed intermittently during the OCP and LPR measurements over 72 h of immersion time in a 3.5 wt-% NaCl solution. The frequency range for EIS measurements was from 100 kHz to 0.01 Hz, with data acquisition occurring at six points per decade. Nyquist and

Bode plots are used to represent the EIS data graphically. The evolution of the polarisation resistance (Rp) of the samples is characterised by the impedance modulus value |Z| at 0.01 Hz ($\Omega.cm^2$) [47,48].

3. Results and discussion

3.1. Microstructural and compositional characterisation of as-received electroless NiP coatings

To study the morphology and chemical composition of the NiP/Cu coatings in top-view and cross-section, SEM/EDS analyses on differently prepared samples were performed. In Fig. 1, top-view and cross-sectional microstructural and compositional analyses of as-received electroless NiP coatings with varying P contents are shown. The EDS spectra of the cross-sectional area of the NP-a, NP-b, and NP-c samples are shown in Fig. 1a_1, a_2, and a_3. The thickness, P content values, average diameter of the nodules, and length of nodular boundaries presented in this study for each sample of the NiP coatings are determined from triplicate cross-sectional EDS line scans, ensuring the reliability and reproducibility of the measurements, as detailed in Table 1. The EDS line scan showed a uniform Ni and P elemental distribution across the thickness, as depicted in Figs. S1, S2, and S3 in the supplementary document.

The SEM/EDS analysis included both a top-view and a cross-sectional perspective. Fig. 1b_1, b_2, and b_3 shows the top-view SEM images of NiP samples with varying P contents. The top-view SEM images show NiP samples with surface nodules of different sizes, as depicted in Fig. 1b_1–b_3. As indicated in Table 2, the order of nodule dimensions, based on the average diameter, is NP-a > NP-b > NP-c. Consequently, the length of nodular boundaries per unit area was calculated in the reverse order of nodular size. Comparing the nodule sizes of the samples reveals that large individual nodules are present for the NP-a sample, resulting in a relatively low nodule boundary density at the surface. With decreasing nodule sizes for the NP-b and NP-c samples, the nodule boundary density increases, respectively. Wang et al. [49] and Dadvand et al. [50] also showed the surface morphological change in NiP alloys as

Table 1
The thickness values, P content, and nodular dimensions of NP-a, NP-b, and NP-c samples.

Electroless NiP coatings	Thickness (μm)	P content (wt%)	Average diameter of the nodules (μm)	Length of nodular boundaries per unit area (μm/μm^2)
NP-a	10.8 ± 0.2	13.2 ± 1.2	14.7 ± 5.1	0.15 ± 0.01
NP-b	9.5 ± 0.1	12.9 ± 0.7	3.8 ± 2.3	0.53 ± 0.01
NP-c	10.0 ± 0.1	8.3 ± 0.8	1.9 ± 0.8	0.78 ± 0.02

Table 2
The VPD difference values (between Cu and NiP coatings) and surface roughness of NP-a, NP-b, and NP-c samples.

Electroless NiP coatings	VPD difference (mV)	Sq (nm)
NP-a	67 ± 2	409 ± 200
NP-b	73 ± 2	111 ± 38
NP-c	150 ± 3	60 ± 15

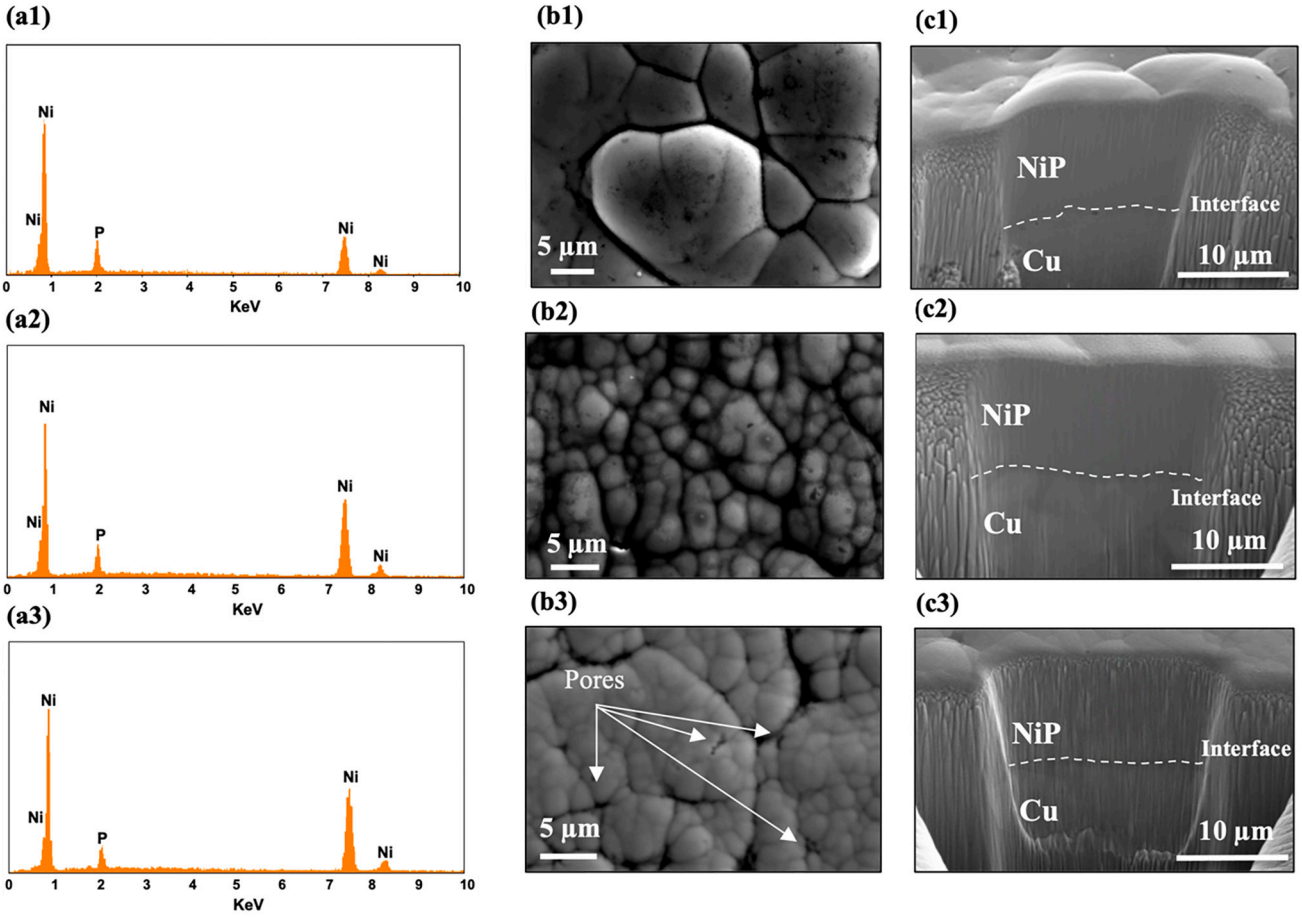

Fig. 1. Microstructural and compositional analysis of the electroless NiP coatings. (a1, a2, a3) representative EDS spectrum acquired on the cross-sectional region of NP-a, NP-b, and NP-c samples, (b1, b2, b3) top-view SEM image of NP-a, NP-b, and NP-c, and (c1, c2, c3) the cross-sectional FIB-SEM image of NP-a, NP-b, and NP-c with the dashed lines indicating the NiP/Cu interface.

the P content increased, with more compact nodules observed in the higher P content specimen. Although the nodule size decreases from NP-a to NP-b samples, the distribution and arrangement of nodules are relatively uniform. In Fig. 1b_3, the NP-c surface exhibits numerous pores/voids, as indicated by the white arrows. These features can be regarded as irregularities along the nodular boundaries, as reported by Shibli and Dilimon [30]. The formation of voids can be attributed to varying plating times, which cause hydrogen bubbles to adsorb on the catalytic surface. These bubbles hinder the growth of new nickel crystals, leading to defects like small pores [51]. They observed that variations in P content within the NiP coatings influence the quality of their surfaces. The study by Shibli and Dilimon [30] revealed that variations in P content within NiP coatings influence surface quality. High P content leads to a uniform, smooth, and amorphous surface; medium phosphorus content results in porous surfaces with distinct grains. Low P content produces porous surfaces with unevenly sized grains and minor flaws such as segregation and voids.

FIB milling was performed to acquire higher-resolution information on the NiP layer thicknesses and the NiP/Cu interface configuration and morphology. Cross-sectional FIB milling of NiP samples (NP-a, NP-b, and NP-c) are shown in Fig. 1c_1, c_2, and c_3. As a generic characteristic of electroless NiP coatings, all cross-sectional images of the samples show a compact structure. Also, they show a flawless interface between the Cu and NiP layers independent of the P content. Variation in the surface morphology of the NiP samples regarding nodule size reveals a distinct correlation between their P content and the nodule size. As is typical of amorphous substances, the NP-a surface exhibits cauliflower-like nodules [34,49,50,52].

XRD measurements were performed to investigate the effect of P content within the NiP coatings on the crystallographic texture of the samples. The P content is a critical factor in determining the microstructure, influencing whether the coating exhibits a crystalline, amorphous, or mixed structure [30]. In Fig. 2, the XRD spectra of the as-plated samples are shown. At sites corresponding to the Ni (111) plane, there was a single large diffraction peak for all samples at a position of 30 to 50°. In the NP-a sample, the corresponding peak to the Ni (111) shows a broad peak profile; however, in the NP-b and NP-c samples, the peak becomes sharper. In the diffraction patterns for the NP-b and NP-c samples, the less intensive peaks corresponding to Ni (200), Ni (311), and Ni (220) are shown; in the NP-a sample the mentioned peaks are difficult to recognize. The sharp peaks marked by the star sign in the plot indicate the Cu substrate. The grain sizes for the samples NP-a, NP-b, and NP-c have been calculated using the Scherrer equation. The grain size values are approximately 20 Å for NP-a, 23 Å for NP-b, and 46 Å for NP-c, respectively. These results are consistent with the study by Choi et al. [53], with observed variations attributable to differences in phosphorus content, deposition parameters, and substrate materials. The P content directly impacts the electrical properties and corrosion resistance performance of the coatings [54,55]. The presence of a broad

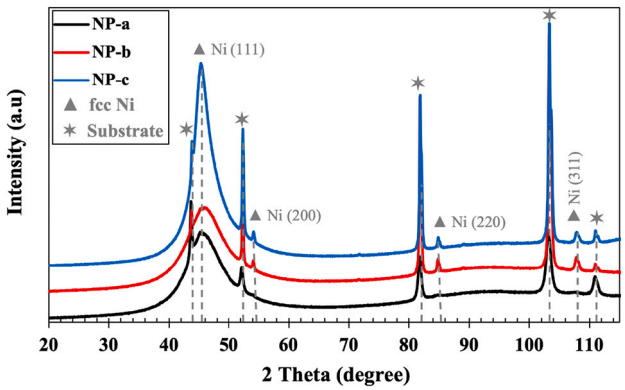

Fig. 2. The XRD patterns from the top surface of NP-a, NP-b, and NP-c.

profile associated with the Ni (111) peak within the range of 30 to 50°, alongside the discernible peaks corresponding to Ni (200), Ni (220), and Ni (311) in all three examined samples, collectively suggests a coexistence of amorphous and nanocrystalline phase structures within the coatings [30,56]. The highly diffused characteristics of the Ni (200), Ni (220), and Ni (311) peaks in the NP-a sample may be attributed to a higher concentration of Ni amorphous phase as opposed to nanocrystalline phase structure. Furthermore, the broadening observed in the Ni (111) peak of the NP-a sample provides additional evidence of a greater proportion of the amorphous phase. Conversely, the discernible peaks related to Ni (200), Ni (220), and Ni (311) in samples NP-b and NP-c can be attributed to the prevalence of a higher proportion of Ni nanocrystalline phase structure relative to the amorphous phase. An increase in phosphorus content results in an increase in lattice strain, which in turn leads to a decrease in grain size, resulting in an amorphous or highly nanocrystalline microstructure [57]. Based on the XRD measurements depicted in Fig. 2 and the grain size calculations conducted on the samples under study; it is inferred that NP-a exhibits a predominantly amorphous (γ) structure, while NP-b and NP-c exhibit a combination of nanocrystalline and amorphous phases (presence of β and γ), with the proportion of nanocrystalline phase increasing from NP-a to NP-b and further to NP-c.

3.2. *Volta potential characterisation of electroless NiP coatings*

The P content in NiP coatings not only affects the crystallinity of the coatings but also can alter the electronic structure of Ni-P alloys as has been reported before [58]. Volta potential characterisation of electroless NiP coatings was carried out to comprehend the impact of phosphorus content. Fig. 3 illustrates the surface topography, amplitude, and VPD mappings of the three samples. The topography and amplitude mappings show the nodules and the distribution of grain boundaries on the surfaces of NiP coatings more clearly. The root mean square (Sq) roughness values obtained from the topography maps are presented in Table 2. There are significant differences in roughness between the samples. The difference in surface roughness and nodular size between the samples can be attributed to variations in nodular growth rate and the number and uniform distribution of nucleation sites, influenced by the local chemical environment during deposition [59].

Fig. 3b3, c3, and d3 depicts the corresponding VPD maps. For the NP-a sample, there is a correlation between potential variations and the large nodules observed in the topography. The highest VPD values are located at both the highest hills of the nodules and the vicinity of nodule boundaries in NP-a and not at the nodule boundaries. However, NP-b exhibits the appearance of higher VPD values at certain nodule boundaries (presented by yellow arrows in Fig. c3). The VPD is more pronounced in the NP-c sample compared to NP-a and NP-b, demonstrating a consistently high VPD at all nodule boundaries and surroundings. This dominant high VPD can be attributed to the smaller size of nodules and lower roughness in NP-c, which has influenced the distribution of surface Volta potential. According to the literature [60,61], localised charges at grain boundaries can create defect states, leading to a bending of energy levels, establishing a contact potential difference (ΔCPD) in the area of nodular boundaries. It is worth noting that the surface potential map of the nodular boundary, detected by the SKPFM probe, represents an electrical grain boundary with a space charge region involving a mixture of surface potential and surface charge rather than crystallographic grain boundaries. This is due to the size of the AFM tip-apex (20 nm), which is larger than the actual grain boundaries. Fig. 3b4, c4, and d4 illustrates the statistical VPD variations along the dashed lines. The lowest VPD values are set to zero to eliminate the possibility of misinterpretation of the VPD maps due to varying measurement conditions across the samples.

The VPD distribution for NP-a is challenging to interpret because of the rough topography of the sample. However, in the case of the NP-b sample (with lower roughness values, which allows us to measure

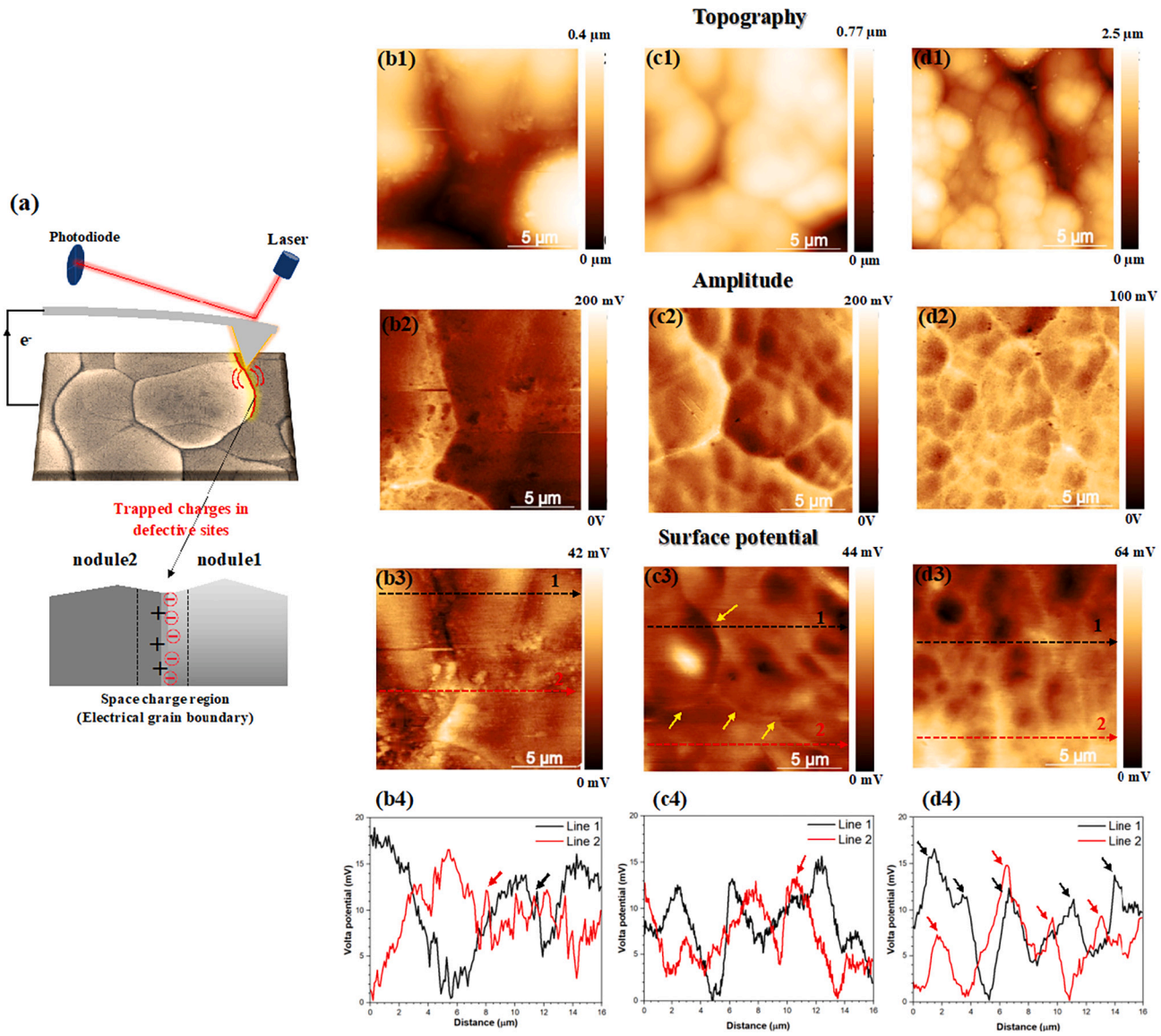

Fig. 3. Surface topography, amplitude, and Volta potential analysis of the electroless NiP coatings. (a) Schematic illustration of internodular SKPFM measurements, (b1, c1, and d1) AFM topography maps of NP-a, NP-b, and NP-c top surface, (b2, c2, and d2) amplitude maps of NP-a, NP-b, and NP-c top surface (b3, c3, and d3) SKPFM maps of NP-a, NP-b, and NP-c top surface, (b4, c4, and d4) variations of VPD values along the dashed lines.

VPD values), slightly higher VPD values observed along the nodular boundaries indicate a higher density of accumulated negative charges in these regions, as schematically shown in Fig. 3a. This suggests a potential vulnerability to corrosion initiation at the nodule boundaries, requiring additional confirmation through electrochemical measurements. It is important to highlight that the difference in VPD values between nodule boundaries and nodules in the NP-b sample is not statistically significant. In contrast, the high VPD values along the nodule boundaries of the NP-c sample may suggest a high density of agglomerated negative charges. When exposed to corrosive media, this can lead to a higher sensitivity to corrosion attack.

Cross-sectional analysis of the Cu/NiP system not only reveals the composition and morphology of the coating but also provides insights into the electronic properties of both NiP and Cu. The electrical connection between layers leads to the equilibration of Fermi levels, causing electrons to migrate from the metal with the lower work function to the metal with the higher work function. Consequently, cross-sectional VPD measurements in this study might indirectly indicate the intrinsic nobility of the layers [46,62]. The cross-sectional topography and VPD mappings of the NP-a, NP-b, and NP-c samples are depicted in Fig. 4. The topographical maps show the cross-section with some light scratches related to polishing. The dashed white lines in the topography maps show the Cu/NiP interface.

Fig. 4b, d, and f depicts the VPD mappings revealing two well-distinct areas attributed to the Cu and NiP layers. NP-a and NP-b samples show almost identical VPD images, and there are no significant differences in potential values between the NP-a and NP-b layers. This can be more clearly depicted in the histogram distribution shown in Fig. 4g, considering the Cu substrate as the reference material. In the case of the NP-c layer, the VPD value is much higher than that of the NP-a and NP-b layers. In summary, low P-containing samples present a larger Volta potential difference with the substrate. This can have significant implications for the corrosion rate of the substrate in the case of defects exposing the Cu underneath. The VPD values between Cu and NiP layers are displayed in Table 2.

It is worth noting that, in correlating corrosion studies with SKPFM studies, variations in work function among microstructural features lead to noticeable differences in Volta potential across the surface, potentially providing insights into their electrochemical characteristics by characterising anodic and cathodic behaviours. The terms “anodic” and

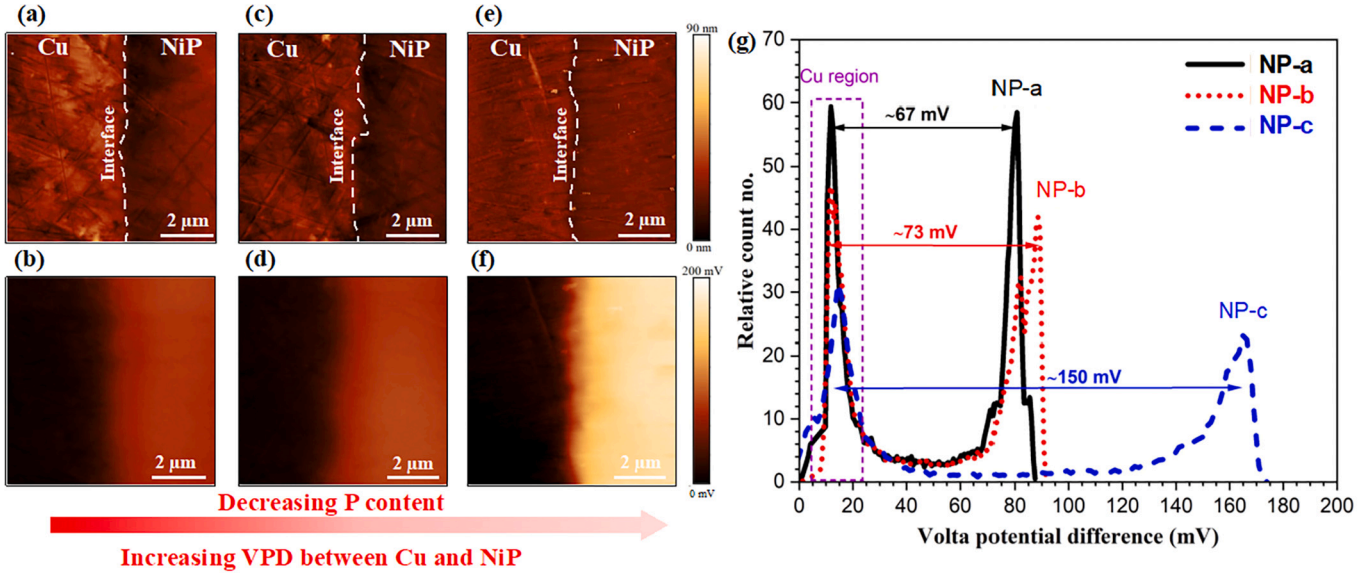

Fig. 4. Cross-sectional AFM morphology and SKPFM volta potential maps, (a, b) NP-a, (c, d) NP-b, and (e, f) NP-c. (g) Histogram distribution of Volta potential difference values in the cross-sectional region of NP-a, NP-b, and NP-c.

"cathodic" are commonly employed concerning Volta potentials, indicating the intrinsic nobility of metals. However, the direct correlation between these potentials and the electrochemical behaviour in actual corrosion scenarios is not always simple. Factors such as environmental condition, alloy composition, and impurities can introduce complexity into the corrosion process. Despite the intrinsically valuable insights offered by theoretical and experimentally measured Volta potentials under atmospheric conditions, their direct correlation with purported corrosion behaviour without scrutinising the experimental conditions can be intricate or even misleading [54,63].

3.3. Electrochemical study of electroless NiP coatings

A combination of destructive and non-destructive electrochemical methods has been employed to investigate the behaviour of NiP coatings. The PDP experiments were conducted in a 3.5 wt-% NaCl solution to evaluate the corrosion behaviour of the samples. In addition, OCP, LPR, and EIS measurements were carried out intermittently in 3.5 wt-% NaCl solution to assess the corrosion properties with exposure time.

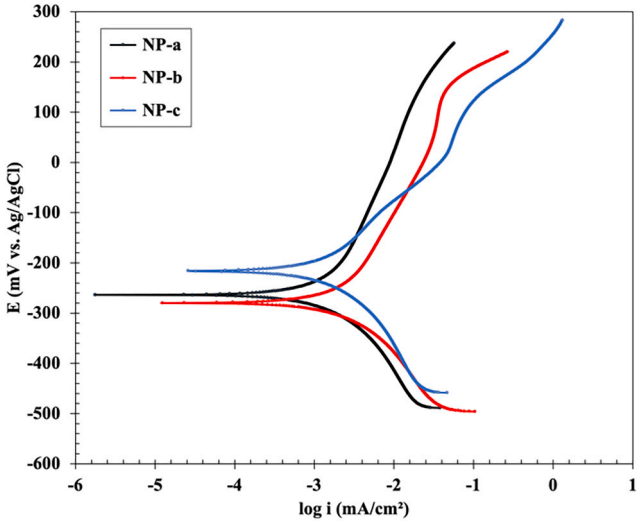

Fig. 5. Potentiodynamic polarisation curves in 3.5 wt-% NaCl solution for the NP-a, NP-b, and NP-c samples.

Fig. 5 shows representative PDP curves for the NP-a, NP-b, and NP-c samples. All cathodic branches exhibit similar behaviour, and the cathodic process is controlled by activation polarisation. Samples NP-a and NP-b showed similar corrosion behaviour in their anodic branches. However, not only does the anodic branch for the NP-a sample show a lower anodic current compared to the NP-b sample, but NP-a also has a steeper anodic slope, indicating that NP-a might exhibit less significant changes in current density values in response to applied anodic polarisation. The distinct increase in current density at higher potentials for NP-b suggests its passive film's instability and propensity for breakdown under anodic polarisation, potentially attributed to microstructural characteristics like roughness and nodular boundary density, facilitating localised film breakdown and transpassive dissolution [64]. On the other hand, the anodic branch of NP-c shows a higher anodic current density and a lower slope compared to NP-a and NP-b. The lower open circuit potential (OCP) values observed in the NP-c sample compared to NP-a and NP-b can be attributed to differences in the passive film characteristics and their stability on the surface. In electroless NiP coatings, a more negative OCP does not necessarily indicate inferior corrosion resistance but rather reflects the electrochemical stability of the surface film. The NP-a sample, characterised by higher phosphorus content, forms a predominantly amorphous structure that promotes the formation of a uniform and protective passive film. This film stabilizes at a more negative potential due to its favorable electrochemical properties. In contrast, NP-c, with lower phosphorus content, exhibits a higher density of nodular boundaries and more pronounced surface Volta potential differences, leading to an uneven charge distribution and reduced corrosion resistance, as evidenced by its lower OCP values. The values for corrosion current density (i_{corr}), anodic Tafel plot slope (βa), and the E_{corr} estimated from Tafel extrapolation are shown in Table 3. The corrosion rate (indicated by the corrosion current density) for the studied samples follows the order: NP-a < NP-b < NP-c.

Table 3
Potentiodynamic polarisation parameter values by Tafel extrapolation for the NP-a, NP-b, and NP-c samples in 3.5 wt-% NaCl solution.

Electroless NiP coatings	i_{corr} (µA/cm^2)	β_a (mV/decade)	E_{corr} (mV vs. Ag/AgCl)
NP-a	1.89 ± 0.08	309 ± 85	−261 ± 54
NP-b	2.19 ± 0.18	277 ± 74	−274 ± 63
NP-c	2.45 ± 0.49	125 ± 26	−218 ± 10

In Fig. 6, the OCP and LPR values for the samples after 72 h of immersion in a 3.5 wt-% NaCl solution are shown. The OCP values are intermittently measured to allow for LPR and EIS measurements. The LPR values are reported at various times of exposure under OCP conditions. As shown in Fig. 6a, although the OCP values for NP-a are higher than those for NP-b (particularly in the first 28 h), NP-a and NP-b OCP values display comparable high or low potential OCP values. On the other hand, the OCP values for NP-c during the 72 h of immersion in 3.5 wt-% NaCl solution consist of three changes in OCP values, i) ~−40 mV (0−10 h), ii) ~+25 mV (10−30 h), and iii) −35 mV (30–72 h). The inset depicts a magnified view of the OCP values throughout the first 10 h of measurements for the samples, indicating that after 4 h of immersion, the NP-c sample showed the lowest OCP values when compared to the NP-a and NP-b samples. The following equation describes the polarisation resistance (Rp) as the primary parameter derived from this method:

$$R_p = \left(\frac{\Delta E}{\Delta i}\right)_{\Delta E \to 0} \quad (3)$$

where ΔE is the polarisation potential and Δi is the polarisation current.

Fig. 7 shows the Nyquist and Bode plots of NP- samples exposed to a 3.5 wt-% NaCl solution for 72 h at various exposure times. Nyquist and Bode plots for NP-a and NP-b are shown in Fig. 7(a, b) and (c, d) respectively. The Nyquist plots show similar behaviour at the same time intervals for the different samples, a single well-defined depressed semicircle. The EIS spectra for the NP-a and NP-b samples indicate that after 2 h of immersion the polarisation resistance (Rp), represented by the impedance modulus value |Z| at 0.01 Hz, increases and subsequently stabilizes with minor fluctuations over time. Fig. 7(e, f) shows the Nyquist plots in NP-c. After 0.5, 1, and 2 h of immersion in a 3.5 wt-% NaCl solution, they exhibit a well-defined depressed semicircle. After 6 and 24 h of exposure to the corrosive media, the plots show a depressed semicircle with an ill-defined tail. They show a single well-defined depressed semicircle again after 48 and 72 h of immersion in 3.5 wt-% NaCl solution with a low Rp. Fig. 8 shows the variation of |Z| values at 0.01 Hz for the samples as a function of exposure time.

In NP-a and NP-b, the rise in polarisation resistance may be attributed to the higher intrinsic corrosion resistance of the natural oxide of the Ni-layer. The elevated resistance of NP-a and NP-b samples could be associated with a uniformly distributed surface charge, as revealed by SKPFM measurements in Fig. 3, thereby promoting the formation of a more protective oxide layer. The nearly identical shape of well-defined semicircles with the same polarisation resistance value in NP-a and NP-b suggests that the corrosion mechanisms are identical, validating the LPR values in Fig. 6b. On the other hand, after 2 h of immersion in a 3.5 wt-% NaCl solution, NP-c exhibited a decreasing trend in polarisation resistance. More than one-time constants in the Nyquist plots suggest a different corrosion mechanism rather than a uniform corrosion [65]. In addition, the decreasing trend of the polarisation resistance value in the NP-c sample validates the LPR values illustrated in Fig. 6b. The lower resistivity observed in NP-c samples may be attributed to an uneven surface Volta potential and/or charge distribution, with higher charge density concentrated in nodular boundaries and lower density in nodular regions, as demonstrated by the SKPFM measurements in Fig. 3. This non-uniform Volta potential and/or charge distribution could render the nodular boundaries more susceptible to corrosion attacks. The corrosion performance of the electroless NiP alloys shows a direct correlation with the P content and nanostructure of the coatings. Therefore, reducing the P content in the nickel electroless process results in smaller nodule sizes or elevated nodule boundaries, characterised by a high level of surface Volta potential heterogeneity and significant charge accumulation at nodule boundaries. This observation further confirms the susceptibility of the NP-c sample to localised corrosion attacks. Additionally, this finding aligns with the polarisation resistance observed in LPR and EIS, where electrochemical signals at the solid/solution interface with the lowest polarisation resistance or resistivity to charge transfer (resulting in the highest i_{corr}) are evident in the NP-c

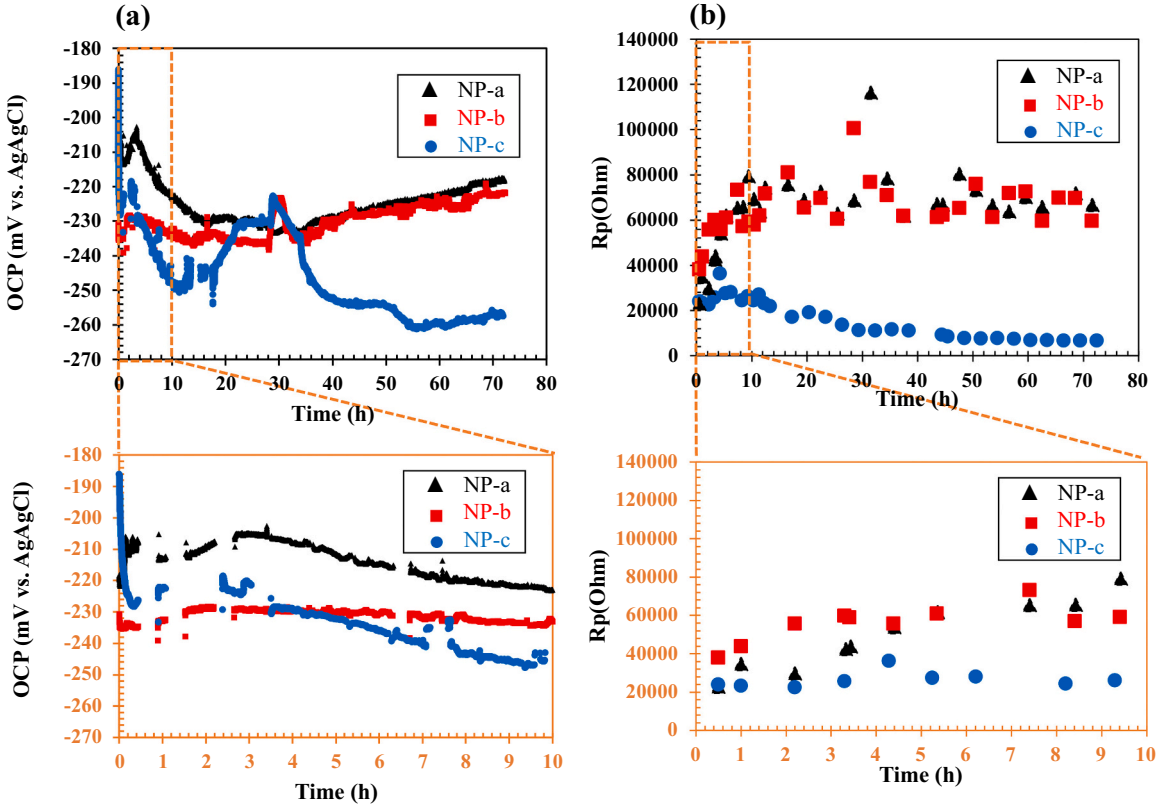

Fig. 6. Electrochemical analysis for NP-a, NP-b, and NP-c samples in 3.5 wt-% NaCl solution over 72 h of immersion (a) OCP, and (b) LPR.

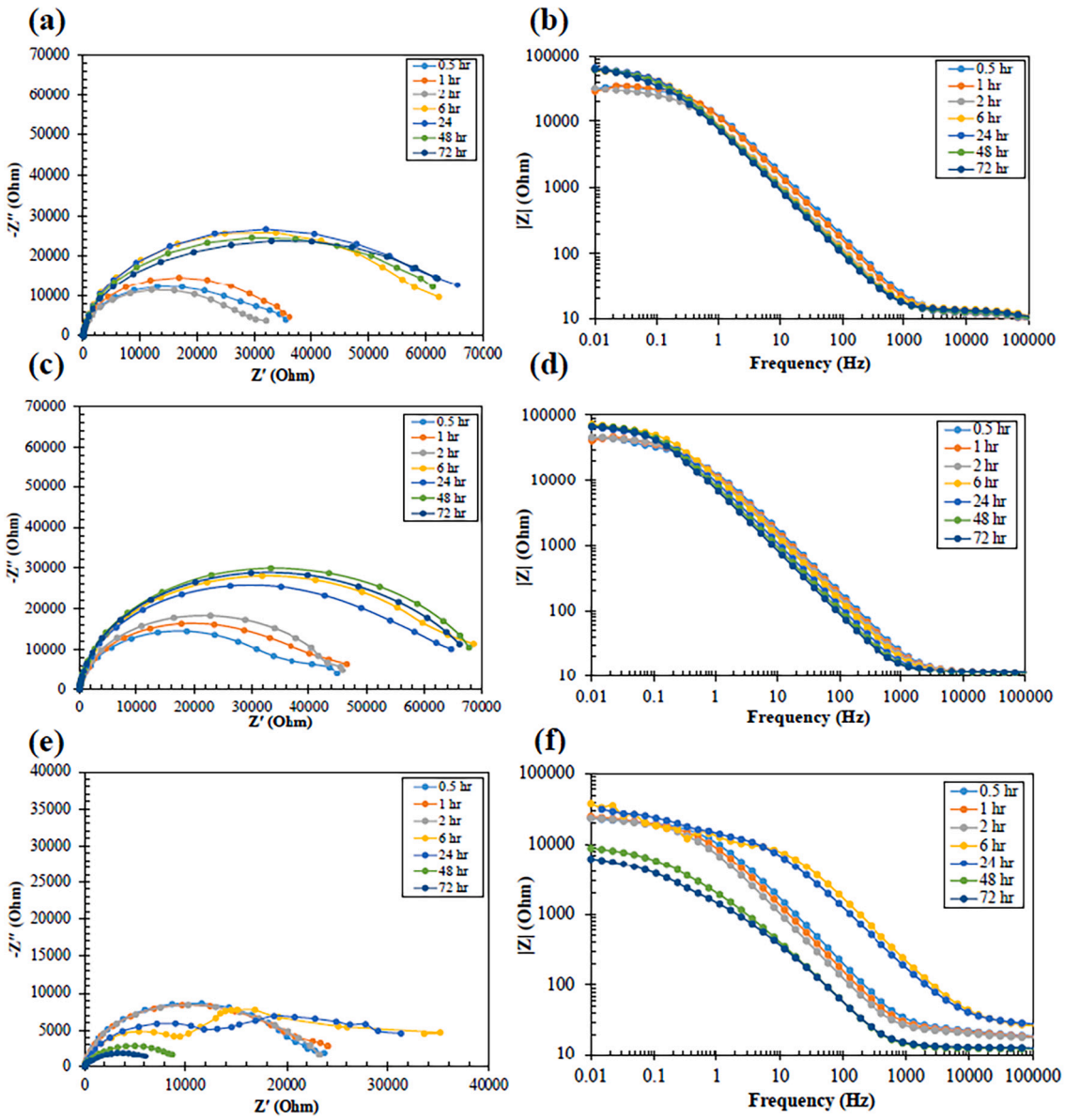

Fig. 7. EIS analysis in 3.5 wt-% NaCl solution over 72 h of immersion: Nyquist and Bode plots (a, b) NP-a, (c, d) NP-b, and (e, f) NP-c.

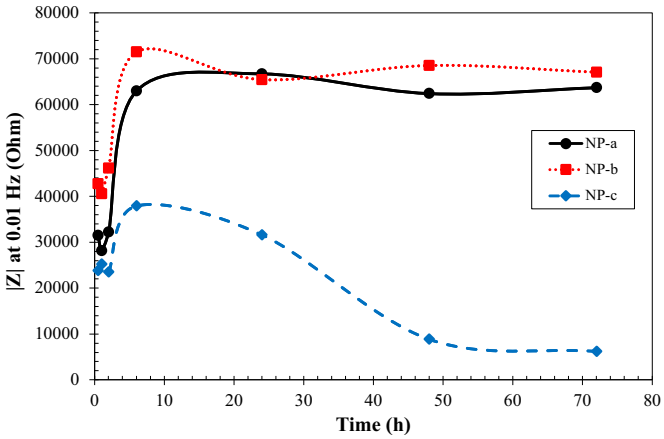

Fig. 8. Electrochemical impedance magnitudes at 0.01 Hz vs. immersion time in 3.5 wt-% NaCl solution over 72 h of immersion.

sample.

3.4. Microstructural and compositional characterisation of post-corroded electroless NiP coatings

In Fig. 9, the top-view SEM/EDS analysis of the samples after 72 h of immersion in the 3.5 wt-% NaCl solution is shown. The low-magnification SEM images of the post-corroded samples after 72 h of immersion are shown in Fig. S4. Fig. 9a and b shows the top-view SEM and EDS mapping analyses of the post-corroded surface of the NP-a and NP-b samples. The post-corroded surfaces of NP-a and NP-b samples show a relatively intact surface. However, Fig. 9c shows a localised corrosion attack for the NP-c sample. The localised corrosion attack in the NP-c sample consists of two types of pits in terms of pit mouth size. The average diameter value for the big pit mouth size is 2.12 ± 0.70 μm, and the pits were formed at the nodule boundaries, and most of the big pits reached the Cu substrate layer. Large pits are indicated by red dashed circles in Fig. 9c. On the other hand, many relatively small pits are distributed mostly on the nodules with an average diameter value of 0.43 ± 0.10 μm.

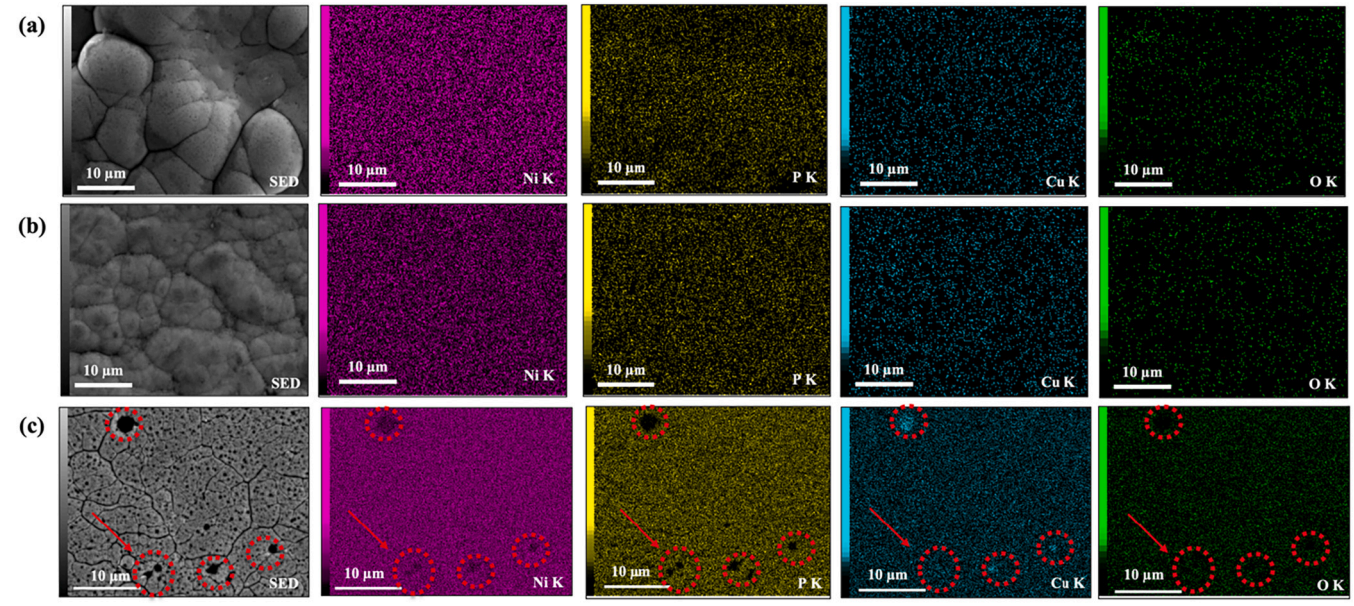

Fig. 9. Top-view SEM image and EDS elemental maps for the post-corroded samples in 3.5 wt-% NaCl, after 72 h of immersion: (a) NP-a, (b) NP-b, and (c) NP-c.

The mostly undamaged post-corroded surfaces of NP-a and NP-b samples demonstrate that the corrosion resistance of the coatings has increased with P content. Due to the coatings' predominantly amorphous structure and uniform charge density distribution, a protective oxide layer may form during the initial immersion. Fig. 5 illustrates wider passive regions for the NP-a and NP-b samples. In contrast, the NP-c sample exhibits poor corrosion behaviour, evident from pit formation attributed to microstructural heterogeneity and a high concentration of negative charge density along the nodular boundaries of the coating with a lower P content [17].

3.5. Corrosion mechanism of electroless NiP coatings

The microstructural, morphological, Volta potential, and electro-

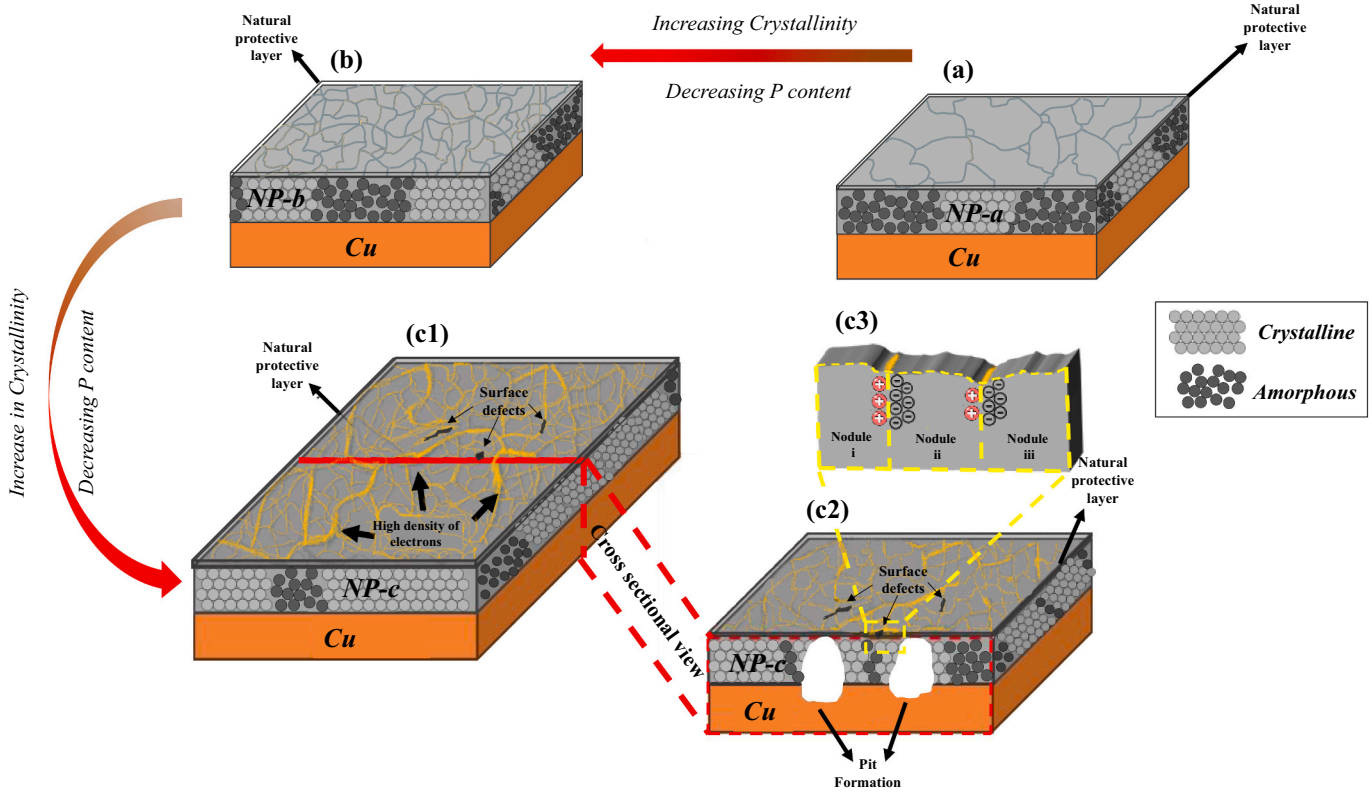

Fig. 10. Schematic illustration of corrosion phenomenon of NP- samples after 72 h of immersion in a 3.5 wt-% NaCl solution (a) NP-a sample, (b) NP-b sample (c1) NP-c sample. (c2) cross-sectional view on red dashed surface area, and (c3) magnified view of the cross-sectional area of NP-c coating showing uneven negative charge density distribution at nodular boundaries. (For interpretation of the references to colour in this figure legend, the reader is referred to the web version of this article.)

chemical analyses reveal that varying P contents significantly influence the corrosion performance of electroless NiP coatings. In NP-a and NP-b samples, high P content induces a shift in the coating microstructure towards a more amorphous phase, forms a lower density of nodular boundaries, provides a sound top surface, and alters the electronic properties of the surface, thereby offering robust corrosion resistance. Nevertheless, in the NP-c samples, the lower P content of the NiP coating leads to increased crystalline phases, a higher density of nodular boundaries, a defective top surface with holes, and an uneven distribution of Volta potential and/or charge distribution on the surface. These factors could potentially result in a less corrosion-resistant performance of the NiP coating in corrosive environments. In Fig. 10, the schematic illustration of the microstructure of all three samples reveals a mixture of amorphous and crystalline phases; however, the ratio of amorphous-to-crystalline order is NP-a > NP-b > NP-c. The microstructural transformation from an amorphous to a crystalline phase by decreasing the P content in NiP layers is shown in Fig. 10. The dark grey disordered atomic arrangement represents the amorphous part, while the light grey ordered lattice structure signifies the crystalline phase. Regarding the morphological characteristics of the top surface of NiP samples, the density of nodular boundaries increases as the P content decreases. Grey lines depict the density of nodular boundaries on the top surface of each sample. Furthermore, NP-a and NP-b exhibit no surface defects, while the NP-c sample displays imperfections such as holes. In terms of the Volta potential properties of the top surface of the three samples, an even negative charge density distribution is evident along the nodular boundaries for the NP-a and NP-b samples, as illustrated in Fig. 10a and b. Conversely, an uneven negative charge density distribution along the nodular boundaries of the NP-c sample is observed in Fig. 10c_1. Determining the uneven negative charge density distribution along the nodular boundaries in NP-c is derived from SKPFM measurements, revealing bright signals in that area. Hence, this high magnitude of surface Volta potential and/or charge distribution in nodule boundaries compared to adjacent nodules may result in a stronger driving force for localised corrosion attack. This can promote rapid corrosion propagation by the accelerated anodic dissolution of the NP-c sample reaching the Cu substrate. However, it is noteworthy that Volta potential difference values along the nodular boundaries in NP-a and NP-b were not significantly different from those in the nodules. To schematically illustrate the corrosion phenomena, NP-a and NP-b samples remained undamaged throughout the immersion period, as depicted in Fig. 10a and b; however, Fig. 10c_1, c_2, and c_3 reveals pit formation in the NP-c sample after 72 h of immersion in a 3.5 wt-% NaCl solution. In Fig. 10c_1, pre-existing surface defects are located at the nodule boundaries, as the black arrows indicate. Additionally, the red line marks the positions of the pores to illustrate the cross-sectional view of the pits in Fig. 10c_2. A thin and weak natural oxide layer might allow corrosive solutions to breach the underlying NiP coating due to susceptible areas along the nodular boundaries in the NP-c sample. Consequently, this breach reaches the copper substrate through localised corrosion attack. Furthermore, the SKPFM cross-sectional study demonstrated that the Volta potential difference values for low P content samples are approximately twice as high as those for high P content samples, likely contributing to a significant galvanic driving force in low P content samples. The possible cathodic reaction (likely on the natural protective layer of the NiP layer) and anodic reactions take place as indicated in Eqs. (4), (5), and (6).

$$O_2 + 2H_2O + 4e^- \longrightarrow 4OH^- \quad (4)$$

$$Ni \longrightarrow Ni^{2+} + 2e^- \quad (5)$$

$$Cu \longrightarrow Cu^{2+} + 2e^- \quad (6)$$

The existence of imperfections and flaws resulting from the low P content allows corrosive solutions to breach the NiP coating, leading to the formation of a high ratio of cathode-to-anode surface area and promoting pit formation. Pitting occurs rapidly due to this high cathode-to-anode surface ratio, driven by the autocatalytic nature of pitting growth and the flaws within the passive layer. Notably, not all pits emerge simultaneously due to variations in electrolyte and surface conditions in different regions [66]. As the P content in NiP alloys decreases, not only does the nanostructure change from a high amorphous/nanocrystalline ratio to a low ratio of amorphous/nanocrystalline regions but also a change in the surface morphology from big to small nodule size. Therefore, the low corrosion performance of low P-content alloys might be correlated to the coatings nanostructure, surface defects, and the abundance of nodule boundaries with high negative charge density as susceptible locations for corrosion initiation. The nanostructural coatings have relatively low corrosion resistance by producing a larger number of micro-galvanic cells between the nodule boundaries and the matrix. On the contrary, an amorphous structure should have intrinsic high corrosion performance owing to its structural homogeneity and the absence of preferential corrosion initiation sites, such as nodule boundaries and other structural flaws [67].

The shape of pit growth in the NP-c sample may differ from the narrow shape suggested in Fig. 10c_2 and could manifest as subsurface, horizontal, or vertical growth. In a prior study, we demonstrated that the direction of electroless Ni dissolution is influenced by system conditions, such as the exposure of microgalvanic couples, the polarisation state, and the acidity and chloride ion (Cl^-) concentration of the solution within the pit [17].

4. Conclusions

This research aims to provide a fundamental understanding of the effect of three different phosphorus contents on the corrosion protection of electroless NiP coatings on a copper substrate in an aqueous chloride-containing environment, specifically focusing on high and low levels of phosphorus content. Interestingly, samples NiP-a and NiP-b, despite having similar P content, exhibited distinct differences in their microstructural properties, particularly in terms of crystallinity. A combination of microstructural, compositional, topographical, local Volta potential distribution and electrochemical studies of as-received electroless NiP coatings allowed for the detailed explanation of localised corrosion phenomena in electroless nickel coatings with varying P content. Decreasing the P content in electroless nickel coatings resulted in minor surface flaws, particularly along the nodular boundaries, associated with a high density of nodular boundaries and a high concentration of negative charge densities. Additionally, it was shown that the Volta potential difference values of low P content samples are approximately twice as high as those of high P content samples, which likely accounts for a large galvanic driving force of low P content samples. The high driving force of low P samples, together with minor surface flaws, resulted in a predominantly localised corrosion attack. The corrosion resistance was found to be in the order of NP-a > NP-b > NP-c for the analysed samples indicating that increasing P content results in a higher corrosion resistance. The difference in corrosion resistance for the NiP coatings with relatively high but similar P content stresses the importance of not only the P content in itself, but in particular its effect on the microstructure of NiP coatings and consequent local corrosion properties.

CRediT authorship contribution statement

M. Mousavi: Writing – original draft, Investigation, Formal analysis, Data curation, Conceptualization. **E. Rahimi:** Writing – review & editing, Investigation, Formal analysis. **J.M.C. Mol:** Writing – review & editing, Supervision, Conceptualization. **Y. Gonzalez-Garcia:** Writing – review & editing, Supervision, Resources, Funding acquisition, Conceptualization.

Declaration of competing interest

The authors declare that they have no known competing financial interests or personal relationships that could have appeared to influence the work reported in this paper.

Data availability

No data was used for the research described in the article.

Acknowledgment

This project has received funding from the European Union's Horizon 2020 research and innovation program under the Marie Skłodowska-Curie grant agreement No. 764977.

Appendix A. Supplementary data

Supplementary data to this article can be found online at https://doi.org/10.1016/j.surfcoat.2024.131174.

References

[1] F. Presuel-Moreno, M.A. Jakab, N. Tailleart, M. Goldman, J.R. Scully, Corrosion-resistant metallic coatings, Mater. Today 11 (2008) 14–23.
[2] J.K. Pancrecious, S.B. Ulaeto, R. Ramya, T.P.D. Rajan, B.C. Pai, Metallic composite coatings by electroless technique–a critical review, Int. Mater. Rev. 63 (2018) 488–512.
[3] C.O. Osifuye, A.P.I. Popoola, C.A. Loto, D.T. Oloruntoba, Effect of Bath parameters on electroless Ni-P and Zn-P deposition on 1045 steel substrate, Int. J. Electrochem. Sci. 9 (2014).
[4] E.M. Fayyad, A.M. Abdullah, M.K. Hassan, A.M. Mohamed, G. Jarjoura, Z. Farhat, Recent advances in electroless-plated Ni-P and its composites for erosion and corrosion applications: a review, Emerg. Mater. 1 (2018) 3–24, https://doi.org/10.1007/s42247-018-0010-4.
[5] C.A. Loto, Electroless nickel plating – a review, Silicon 8 (2016) 177–186, https://doi.org/10.1007/s12633-015-9367-7.
[6] M. Molaei, M. Atapour, Nickel-based coatings as highly active electrocatalysts for hydrogen evolution reaction: a review on electroless plating cost-effective technique, sustainable, Mater. Technol. 40 (2024) e00991.
[7] B.-H. Shin, J. Park, S. Kim, J.-W. Ok, D.-I. Kim, J.-H. Yoon, Study of electroless nickel plating on super duplex stainless steel for lithium-ion battery cases: electrochemical behaviour and effects of plating time, Metals 14 (2024) 307.
[8] P.J. Sharma, K.H. Modi, P. Sahatiya, C.K. Sumesh, P.M. Pataniya, Electroless deposited NiP-fabric electrodes for efficient water and urea electrolysis for hydrogen production at industrial scale, Appl. Surf. Sci. 644 (2024) 158766.
[9] M.L. Et. Al, Investigations on surface behavior of electro-less nickel phosphorus coatings with nano additives on magnesium alloy used in automotive applications, PAE 58 (2021) 4020–4028, https://doi.org/10.17762/pae.v58i3.4609.
[10] N. Ghavidel, S.R. Allahkaram, R. Naderi, M. Barzegar, H. Bakhshandeh, Corrosion and wear behavior of an electroless Ni-P/nano-SiC coating on AZ31 Mg alloy obtained through environmentally-friendly conversion coating, Surf. Coat. Technol. 382 (2020) 125156, https://doi.org/10.1016/j.surfcoat.2019.125156.
[11] A. Thakur, S. Gharde, B. Kandasubramanian, Electroless nickel fabrication on surface modified magnesium substrates, Def. Technol. 15 (2019) 636–644, https://doi.org/10.1016/j.dt.2019.04.006.
[12] Z. Huang, Q. Yong, Z.-H. Xie, Stearic acid modified porous nickel-based coating on magnesium alloy AZ31 for high superhydrophobicity and corrosion resistance, corrosion, Communications 10 (2023) 38–47.
[13] C. Cui, H. Du, H. Liu, T. Xiong, Corrosion behavior of the electroless Ni-P coating on the pore walls of the lotus-type porous copper, Corros. Sci. 162 (2020) 108202, https://doi.org/10.1016/j.corsci.2019.108202.
[14] C. Sun, J. Li, V. Fattahpour, M. Roostaei, M. Mahmoudi, H. Zeng, J.-L. Luo, Insights into the erosion-enhanced corrosion on electroless Ni–P coating from single particle impingement, Corros. Sci. 166 (2020) 108422, https://doi.org/10.1016/j.corsci.2019.108422.
[15] E.F. Monlevade, I.A.P. Cardoso, E.F.L. Maciel, N. Alonso-Falleiros, Galvanic corrosion of electroless nickel/immersion gold plated non-permanent electric contacts used in electronic devices–direct evidence of triggering mechanism, Eng. Fail. Anal. 96 (2019) 562–569, https://doi.org/10.1016/j.engfailanal.2018.12.001.
[16] A. Bahramian, M. Eyraud, S. Maria, F. Vacandio, T. Djenizian, P. Knauth, Enhancing the corrosion resistance of Cu/Ni-P/Au electrical contacts by electropolymerized poly(methyl methacrylate), Corros. Sci. 149 (2019) 75–86, https://doi.org/10.1016/j.corsci.2018.12.026.
[17] M. Mousavi, A. Kosari, J.M.C. Mol, Y. Gonzalez-Garcia, Localised aqueous corrosion of electroless nickel immersion gold-coated copper, Corros. Eng. Sci. Technol. 57 (2022) 520–530, https://doi.org/10.1080/1478422X.2022.2096322.
[18] V.K. Murugan, Z. Jia, G.J. Syaranamual, C.L. Gan, Y. Huang, Z. Chen, Atmospheric corrosion resistance of electroplated Ni/Ni–P/Au electronic contacts, Microelectron. Reliab. 60 (2016) 84–92, https://doi.org/10.1016/j.microrel.2016.02.014.
[19] Y.-H. Lee, S.-R. Choi, S.-J. Ko, J.-G. Kim, Effect of benzotriazole on the prevention of electroless nickel–immersion gold treated copper corrosion, J. Phys. Chem. Solid 176 (2023) 111226, https://doi.org/10.1016/j.jpcs.2023.111226.
[20] A. Khaira, I. Shown, S. Samireddi, S. Mukhopadhyay, S. Chatterjee, Mechanical and tribological characterization of deep eutectic solvent assisted electroless Ni–P-hBN coating, Ceram. Int. 49 (2023) 461–473.
[21] M.N. Collins, M. Reid, E. Dalton, K. Shannon, L.F. Garfias-Mesias, Corrosion under mixed flowing gas conditions of various connector coatings: mixed flowing gas (MFG) corrosion, Mater. Corros. 64 (2013) 7–13, https://doi.org/10.1002/maco.201106340.
[22] A. Ballantyne, G. Forrest, M. Goosey, A. Griguceviciene, J. Juodkazyte, R. Kellner, A. Kosenko, R. Ramanauskas, K. Ryder, A. Selskis, R. Tarozaite, E. Veninga, Advanced surface protection for improved reliability PCB systems (ASPIS), Circuit World 38 (2012) 21–29, https://doi.org/10.1108/03056121211195021.
[23] T.S.N. Sankara Narayanan, I. Baskaran, K. Krishnaveni, S. Parthiban, Deposition of electroless Ni–P graded coatings and evaluation of their corrosion resistance, Surf. Coat. Technol. 200 (2006) 3438–3445, https://doi.org/10.1016/j.surfcoat.2004.10.014.
[24] I.A. Shozib, A. Ahmad, A.M. Abdul-Rani, M. Beheshti, A.A. Aliyu, A review on the corrosion resistance of electroless Ni-P based composite coatings and electrochemical corrosion testing methods, Corrosion Rev. 40 (2022) 1–37, https://doi.org/10.1515/corrrev-2020-0091.
[25] G. Pedrizzetti, L. Paglia, V. Genova, S. Cinotti, M. Bellacci, F. Marra, G. Pulci, Microstructural, mechanical and corrosion characterization of electroless Ni-P composite coatings modified with ZrO2 reinforcing nanoparticles, Surf. Coat. Technol. 473 (2023) 129981.
[26] H. Nazari, G. Barati Darband, R. Arefinia, A review on electroless Ni–P nanocomposite coatings: effect of hard, soft, and synergistic nanoparticles, J. Mater. Sci. 58 (2023) 4292–4358.
[27] S.W. Court, B.D. Barker, F.C. Walsh, Electrochemical measurements of electroless nickel coatings on zincated aluminium substrates, Trans. IMF 78 (2000) 157–162, https://doi.org/10.1080/00202967.2000.11871330.
[28] F. Bigdeli, S.R. Allahkaram, An investigation on corrosion resistance of as-applied and heat treated Ni–P/nanoSiC coatings, Mater. Des. 30 (2009) 4450–4453, https://doi.org/10.1016/j.matdes.2009.04.020.
[30] S.M.A. Shibli, V.S. Dilimon, Effect of phosphorous content and TiO2TiO2-reinforcement on Ni–P electroless plates for hydrogen evolution reaction, Int. J. Hydrogen Energy 32 (2007) 1694–1700, https://doi.org/10.1016/j.ijhydene.2006.11.037.
[31] A.S. Hamada, P. Sahu, D.A. Porter, Indentation property and corrosion resistance of electroless nickel–phosphorus coatings deposited on austenitic high-Mn TWIP steel, Appl. Surf. Sci. 356 (2015) 1–8.
[32] V. Vitry, A. Sens, A.-F. Kanta, F. Delaunois, Wear and corrosion resistance of heat treated and as-plated Duplex NiP/NiB coatings on 2024 aluminum alloys, Surf. Coat. Technol. 206 (2012) 3421–3427.
[33] A. Bai, P.-Y. Chuang, C.-C. Hu, The corrosion behavior of Ni–P deposits with high phosphorous contents in brine media, Mater. Chem. Phys. 82 (2003) 93–100, https://doi.org/10.1016/S0254-0584(03)00193-7.
[34] G. Lu, Corrosion resistance of ternary Ni Ã/P based alloys in sulfuric acid solutions, Electrochim. Acta 11 (2002).
[35] L. Bonin, V. Vitry, F. Delaunois, Corrosion behaviour of electroless high boron-mid phosphorous nickel duplex coatings in the as-plated and heat-treated states in NaCl, H2SO4, NaOH and Na2SO4 media, Mater. Chem. Phys. 208 (2018) 77–84, https://doi.org/10.1016/j.matchemphys.2017.12.030.
[36] J. Sudagar, J. Lian, W. Sha, Electroless nickel, alloy, composite and nano coatings – a critical review, J. Alloys Compd. 571 (2013) 183–204, https://doi.org/10.1016/j.jallcom.2013.03.107.
[37] V.B. Chintada, R. Koona, Preparation and properties of composite electroless Ni-P-ZnO coatings, Mater. Res. Innov. 24 (2020) 67–74, https://doi.org/10.1080/14328917.2019.1582740.
[38] F. Nabhan, E.M. Fayyad, M.H. Sliem, F.M. Shurrab, K. Eid, G. Nasrallah, A. M. Abdullah, ZnO-doped gC3N4 nanocapsules for enhancing the performance of electroless NiP coating— mechanical, corrosion protection, and antibacterial properties, ACS Omega 8 (2023) 22361–22381.
[39] P. Pandian, P. Sundaram, A. Sathishkumar, R. Prabakaran, P.G. Kumar, S.C. Kim, A. Alodhayb, S. Pandiaraj, E. Rasu, M. Rajaraman, Effect of sodium dodecyl sulfate surfactant on the surface properties of electroless NiP-TiO2-ZrO2 composite coatings on magnesium AZ91D substrate, Arab. J. Chem. 16 (2023) 105028.
[40] R. Jensen, Z. Farhat, M.A. Islam, G. Jarjoura, Erosion–Corrosion of Novel Electroless Ni-P-NiTi Composite Coating, Corros. Mater. Degrad. 4 (2023) 120–141.
[41] W. Yan, C. Tiejun, Z. Ruihong, Electroless deposition of NiMoP coating on Q235B steel and its corrosion resistance in simulated concrete pore solution, Int. J. Electrochem. Sci. 18 (2023) 100313.
[42] J. Zhong, S. Zhang, Y. He, Y. Fan, Z. Li, L. Yan, H. Zhou, X. Cheng, J. Song, H. Li, Study on the use of furan epoxide modified graphene to enhance the corrosion resistance and wear resistance of electroless Ni-WP coatings, Surf. Coat. Technol. 473 (2023) 129946.
[43] N. Jadhav, V.J. Gelling, Review—the use of localized electrochemical techniques for corrosion studies, J. Electrochem. Soc. 166 (2019) C3461–C3476, https://doi.org/10.1149/2.0541911jes.

[44] N.E. Benaioun, N. Moulayat, N.E. Hakiki, H. Ramdane, E. Denys, A. Florentin, K. D. Khodja, M.M. Heireche, J.L. Bubendorff, Passive films formed on Fe- and Ni-based alloys in an alkaline medium: an insight into complementarities between electrochemical techniques and near-field microscopies (AFM/SKPFM), Appl. Sci. 13 (2023) 11659, https://doi.org/10.3390/app132111659.
[45] J. León, B. Ter-Ovanessian, B. Normand, H. Terryn, B. Özkaya, M. Lekka, H.-J. Grande, E. García-Lecina, J.M. Vega, Corrosion resistance of electroplated coatings based on chromium trivalent-baths, Surf. Coat. Technol. 481 (2024) 130616, https://doi.org/10.1016/j.surfcoat.2024.130616.
[46] C. Örnek, C. Leygraf, J. Pan, On the Volta potential measured by SKPFM – fundamental and practical aspects with relevance to corrosion science, Corros. Eng. Sci. Technol. 54 (2019) 185–198, https://doi.org/10.1080/1478422X.2019.1583436.
[47] J. Li, R. Wu, Z. Jing, L. Yan, F. Zha, Z. Lei, One-step spray-coating process for the fabrication of colorful superhydrophobic coatings with excellent corrosion resistance, Langmuir 31 (2015) 10702–10707, https://doi.org/10.1021/acs.langmuir.5b02734.
[48] A.R. Rahimi, H. Modarres, M. Abdouss, Study on morphology and corrosion resistance of electroless Ni–P coatings, Surf. Eng. 25 (2009) 367–371, https://doi.org/10.1179/174329409X379273.
[49] X.-C. Wang, W.-B. Cai, W.-J. Wang, H.-T. Liu, Z.-Z. Yu, Effects of ligands on electroless Ni–P alloy plating from alkaline citrate–ammonia solution, Surf. Coat. Technol. 168 (2003) 300–306, https://doi.org/10.1016/S0257-8972(03)00013-6.
[50] N. Dadvand, W.F. Caley, G.J. Kipouros, Effect of microstructure and phosphorus content on the corrosion behaviour of electroless nickel-phosphorus coatings, Can. Metall. Quart. 45 (n.d.) 8.
[51] A. Salicio-Paz, H. Grande, E. Pellicer, J. Sort, J. Fornell, R. Offoiach, M. Lekka, E. García-Lecina, Monolayered versus multilayered electroless NiP coatings: impact of the plating approach on the microstructure, mechanical and corrosion properties of the coatings, Surf. Coat. Technol. 368 (2019) 138–146, https://doi.org/10.1016/j.surfcoat.2019.04.013.
[52] Y.D. He, H.F. Fu, X.G. Li, W. Gao, Microstructure and properties of mechanical attrition enhanced electroless Ni–P plating on magnesium alloy, Scr. Mater. 58 (2008) 504–507, https://doi.org/10.1016/j.scriptamat.2007.10.051.
[53] B.-K. Choi, S.-J. Park, M.-K. Seo, Effect of processing parameters on the thermal and electrical properties of electroless nickel-phosphorus plated carbon Fiber heating elements, C 6 (2020) 6, https://doi.org/10.3390/c6010006.
[54] C.M. Efaw, T. da Silva, P.H. Davis, L. Li, E. Graugnard, M.F. Hurley, Toward improving ambient volta potential measurements with SKPFM for corrosion studies, J. Electrochem. Soc. 166 (2019) C3018–C3027, https://doi.org/10.1149/2.0041911jes.
[55] H. Ashassi-Sorkhabi, S.H. Rafizadeh, Effect of coating time and heat treatment on structures and corrosion characteristics of electroless Ni–P alloy deposits, Surf. Coat. Technol. 176 (2004) 318–326.
[56] J. Li, C. Sun, M. Roostaei, M. Mahmoudi, V. Fattahpour, H. Zeng, J.-L. Luo, Insights into the electrochemical corrosion behavior and mechanism of electroless Ni-P coating in the CO2/H2S/Cl− environment, Corrosion 76 (2020) 578–590, https://doi.org/10.5006/3371.
[57] D.R. Dhakal, G. Gyawali, Y.K. Kshetri, J.-H. Choi, S.W. Lee, Microstructural and electrochemical corrosion properties of electroless Ni-P-TaC composite coating, Surf. Coat. Technol. 381 (2020) 125135, https://doi.org/10.1016/j.surfcoat.2019.125135.
[58] B. Elsener, D. Atzei, A. Krolikowski, A. Rossi, Effect of phosphorus concentration on the electronic structure of nanocrystalline electrodeposited Ni–P alloys: an XPS and XAES investigation, Surf. Interface Anal. 40 (2008) 919–926, https://doi.org/10.1002/sia.2802.
[59] P. Sahoo, Optimization of electroless Ni-P coatings based on multiple roughness characteristics, Surf. Interface Anal. 40 (2008) 1552–1561, https://doi.org/10.1002/sia.2945.
[60] J. Gonzalez-Julian, K. Neuhaus, M. Bernemann, J. Pereira Da Silva, A. Laptev, M. Bram, O. Guillon, Unveiling the mechanisms of cold sintering of ZnO at 250 °C by varying applied stress and characterizing grain boundaries by kelvin probe force microscopy, Acta Mater. 144 (2018) 116–128, https://doi.org/10.1016/j.actamat.2017.10.055.
[61] T.-X. Qin, E.-M. You, M.-X. Zhang, P. Zheng, X.-F. Huang, S.-Y. Ding, B.-W. Mao, Z.-Q. Tian, Quantification of electron accumulation at grain boundaries in perovskite polycrystalline films by correlative infrared-spectroscopic nanoimaging and Kelvin probe force microscopy, Light Sci. Appl. 10 (2021) 84, https://doi.org/10.1038/s41377-021-00524-7.
[62] T. Pan, Z. Wang, A polyaniline based intrinsically conducting coating for corrosion protection of structural steels, Microsc. Res. Tech. 76 (2013) 1186–1195, https://doi.org/10.1002/jemt.22283.
[63] C. Örnek, D.L. Engelberg, An experimental investigation into strain and stress partitioning of duplex stainless steel using digital image correlation, X-ray diffraction and scanning Kelvin probe force microscopy, the, J. Strain Anal. Eng. Des. 51 (2016) 207–219, https://doi.org/10.1177/0309324716631669.
[64] H. Luo, M. Leitch, Y. Behnamian, Y. Ma, H. Zeng, J.-L. Luo, Development of electroless Ni–P/nano-WC composite coatings and investigation on its properties, Surf. Coat. Technol. 277 (2015) 99–106, https://doi.org/10.1016/j.surfcoat.2015.07.011.
[65] M. Arnaudova, E. Lefterova, R. Rashkov, Corrosion behavior of electrodeposited nickel-based coatings with W, Mo, and TiOx, J. Solid State Electrochem. (2023) 1–14.
[66] V.K. Murugan, Z. Jia, G.J. Syaranamual, C.L. Gan, Y. Huang, Z. Chen, An investigation into different nickel and nickel–phosphorus stacked thin coatings for the corrosion protection of electrical contacts, Surf. Coat. Technol. 300 (2016) 95–103, https://doi.org/10.1016/j.surfcoat.2016.05.013.
[67] Y. Gao, Z.J. Zheng, M. Zhu, C.P. Luo, Corrosion resistance of electrolessly deposited Ni–P and Ni–W–P alloys with various structures, Mater. Sci. Eng. A 381 (2004) 98–103, https://doi.org/10.1016/j.msea.2004.04.077.